Journal of Engineering Mathematics **48:** 375–389, 2004.

Computations of bubble formation and pulsations generated by impacting cylindrical water jets

WILLIAM G. SZYMCZAK, STEVEN L. MEANS[1] and JOEL C. W. ROGERS[2]
Code 7131, Naval Research Laboratory, 4555 Overlook Drive SW., Washington, DC 20375, USA (e-mail: szymczak@nrl.navy.mil); [1]*Code 7121, Naval Research Laboratory, 4555 Overlook Drive SW., Washington, DC 20375, USA (e-mail: means@wave.nrl.navy.mil);* [2]*Department of Applied Mathematics and Physics, Polytechnic University, Brooklyn, NY 11201, USA (e-mail: JCWRogers@earthlink.net)*

Received 2 January 2003; accepted in revised form 25 June 2003

Abstract. The impact of a water jet onto a water surface can entrain air-bubbles whose pulsations provide acoustic sources. Such impacts can occur during the breaking of a wave, or on a smaller scale, when a raindrop strikes a puddle of water. A better understanding of this phenomenon can lead to improved characterizations of the ambient noise and acoustic detection algorithms. Liquid on liquid impacts correspond to a breakdown of classical hydrodynamic theory which assumes that the free surface remains smooth and topologically invariant. A computational model using a generalized theory of hydrodynamics designed to rigorously treat liquid collisions is described in this paper. Numerical simulations are compared to experiments of a liquid cylinder impacting a still-water surface The simulations provide details not only of the initial formation of the air-entrained bubble at the time of the cavity collapse, but also the subsequent pulsations of this bubble until it rises back to the free surface. Computed initial bubble sizes and natural frequencies are compared to the experimental results for different cylinder lengths.

Key words: bubble pulsations, liquid cylinder, liquid impacts

1. Introduction

One of the most familiar examples of liquid impacts is the breaking of an ocean wave. The bubbles formed during this violent motion create phenomena important in many different fields. As described in [1] and [2] applications include global climate modeling through the enhanced absorption of gases across the ocean surface or the release of marine aerosols into the atmosphere. Another potential application is the enhancement of acoustic detection algorithms through improved characterization of the ambient noise. This application, in particular the characterization of low-frequency noise caused by air entrainment in breaking waves, provides the motivation for this study. While a direct simulation resolving all the turbulent scales of wave breaking is not feasible, we begin with an idealized experiment of a falling cylinder of water onto a still water surface.

The experimental setup described in [3] is displayed in Figure 1. In particular, the case when $R = 5{\cdot}4$ cm, $H = 15$ cm, will be considered with lengths ranging from $L = 15$ cm to $L = 45$ cm. In the experiments, Kolaini *et al.* [3] measured the pressure time history at a fixed location under the water and determined the resonant frequencies of the bubble. It was found that the frequency was inversely proportional to the initial bubble plume radius. Numerical predictions of these experiments have been reported in [4] using a boundary-element method (BEM). While this procedure was able to accurately predict the initial bubble size, it was unable to simulate the subsequent bubble pulsations and hence dominant frequency of the

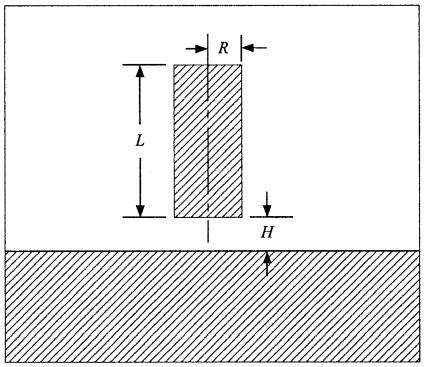

Figure 1. Experimental setup of a liquid cylinder above still water.

bubble. The reason for the failure of the BEM on this problem is due to the many topological changes occuring during the bubble pulsations. Each topology change is associated with different portions of the free surface colliding, and each collision causes a singularity in the BEM which must be carefully treated (see *e.g.* [5] or [6]). These methodologies for removing singularities are dependent on *a priori* knowledge of the nature of the topology change. While it may be possible to use a BEM past the time of the initial cavity closure, (to our knowledge, this has not yet been done for this problem) simulating the subsequent jetting, splitting, and re-merging of the bubbles while they are pulsating is not feasible with that approach.

A detailed numerical investigation of the related problem of impacting drops was performed in [7] using a Volume of Fluid (VOF) approach. Unlike the method in [4], this approach was able to predict thin high speed jets that often form on the collapse of the cavity. However, their model did not include a treatment of the air entrained in the bubble, and consequently, was unable to simulate bubble pulsations.

A generalized formulation of hydrodynamics capable of treating the singularities caused by liquid collisions is used in this study. While this approach may be classified as a VOF method, there are some important differences which are discussed in the next section. Details of the model and its numerical implementation may be found in [8–11]. The computer code implementing this model for both axially symmetric and two-dimensional problems is called BUB2D. A separate code, BUB3D is used for three-dimensional problems. One of the benchmarks for validating this model was the collision of two incompressible liquid cylinders. This benchmark was discussed in detail in [11] and [12] for concentric cylinders with the same radii, and with cylinders of different radii in [13]. Other applications of these codes include underwater bubble dynamics, shallow-depth plume formation [13–15], explosive cratering in water-covered sand [16] and [17], and preliminary results in wave breaking [17]. In general, the strength of this approach is the ability to simulate long-time violent free-surface phenomena, such as those encountered when a bubble undergoes multiple oscillations. Its weaknesses include its first-order accurate representation of the free surface, which can become slightly smeared due to numerical effects, even during stable motions.

Whereas the previous attempts of [4] and [7] have only been able to address the early stages of this cylinder-impact problem, simulations of both the air entrainment and subsequent bubble pulsations are presented in this paper. The simulated bubble sizes and pulsation frequencies are compared to the experiments of [3].

2. Model description

The generalized hydrodynamic model is based on a constrained system of conservation laws. The equations are

$$(\rho \mathbf{u})_t + \nabla \cdot (\rho \mathbf{u}\mathbf{u}) = -\rho g \mathbf{k} - \nabla P, \tag{1}$$

$$\rho_t + \nabla \cdot (\rho \mathbf{u}) = 0, \qquad \text{for } \mathbf{x} \in \Omega, \tag{2}$$

subject to the constraint

$$\rho \leq \rho_0. \tag{3}$$

In this formulation the density acts as a volume of fluid variable and the liquid region is defined by $\mathbf{D}(t) = \{\mathbf{x} \in \Omega : \rho(\mathbf{x}, t) = \rho_0\}$. In each connected, disjoint subset of the non-liquid region, $\Omega - \mathbf{D}(\mathbf{t})$, the pressure is assumed to be uniform. For example, in the atmospheric region above the liquid the pressure is set to the ambient air pressure. In an underwater bubble, the pressure P_B may be determined using the adiabatic law $P_B = C {V_B}^{-\gamma}$, where V_B is the bubble volume, C is a constant, and γ is the ratio of specific heats of the bubble gases. Since the pressure is continuous in the absence of surface tension and viscosity, these values can be treated as boundary conditions for determining the pressure in $\mathbf{D}(t)$. Note, that this formulation allows for regions of 'spray' in the non-liquid region where $0 < \rho < \rho_0$. Such regions are not allowed in potential flow formulations such as the one used in [4] and the references cited therein, where the flow is assumed to be delineated so that either $\rho = \rho_0$ or $\rho = 0$. They are also suppressed in the VOF methods described in [18], [19] and [7], among others, where the fluid volume variable is constrained to take values from the discrete set $\{0, 1\}$. Regions of spray can be expected to form when the free surfaces become unstable, in particular when Rayleigh-Taylor instabilities occur. Since these instabilities often occur during violent free surface dynamics, we do not *a priori* suppress spray regions through the use of any type of surface-tracking or special level-set approaches. Furthermore, while the liquid region is assumed to be incompressible due to the constraint (3), no additional irrotational assumption is made.

Solutions to the constrained system (1)–(3) are approximated using a split step algorithm which advances the flow variables $\rho^n, \mathbf{u}^n, P^n$ at time t^n, to the flow $\rho^{n+1}, \mathbf{u}^{n+1}, P^{n+1}$ at time $t^{n+1} = t^n + \tau$.

The first step of the algorithm solves (1) and (2) approximately, without the pressure gradient in the momentum equation and without regard to the constraint (3) for the time τ, yielding a flow $(\tilde{\rho}, \tilde{\mathbf{u}})$. In the continuous (in space) algorithm, the solution to these equations may be approximated by the solution to a 'collisionless Boltzmann equation' as described in [13]. Numerically, this step is approximated using a second-order, monotone-upwinded Godunov method where approximations to the discrete Riemann problems are consistent with inelastic collisions when characteristics cross. Details of this algorithm for axially symmetric problems were given in [11]. The monotonicity of this scheme has the effect of implicitly adding artificial viscosity in regions where the velocity gradients are rapidly changing. A discussion of how such algorithms may be considered as Monotone Implicit Large Eddy Simulations (MILES) for the treatment of turbulence may be found in [20] and [21].

The second step of the algorithm redistributes the excess of $\tilde{\rho}$ over ρ_0 and corrects the velocity field $\tilde{\mathbf{u}}$ such that mass and momentum is conserved, and the energy cannot increase. This

step represents another distinguishing feature of our model from the VOF models previously mentioned, which simply truncate any excesses. In addition to violating mass conservation, such strategies will in general violate momentum conservation and can lead to small energy increases. The excess density is redistributed by setting

$$\rho^{n+1} = \tilde{\rho} + \nabla^2 H, \tag{4}$$

where $H > 0$ is the solution of the 'obstacle problem'

$$\nabla^2 H = \begin{cases} \rho_0 - \tilde{\rho} & \text{if } H > 0 \\ 0 & \text{if } H = 0 \end{cases}. \tag{5}$$

Note that (5) and (4) imply that $\rho^{n+1} \leq \rho_0$ in the entire domain.

Associated with the density redistribution the velocity (momentum) is redistributed by solving

$$\rho^{n+1}\overline{\mathbf{u}} = \tilde{\rho}\tilde{\mathbf{u}} + \nabla^2(\overline{\mathbf{u}}H). \tag{6}$$

This redistribution strategy was derived by considering the steady state solution to a 'Stefan-Boltzmann' equation. A description of this derivation may be found in [13]. A discretization of (5) yields a discrete linear complementarity problem. This nonlinear system is solved using a constrained conjugate gradient method with diagonal or incomplete Choleski preconditioning. Details of this algorithm were presented in [11]. The momentum-redistribution equation (6) is first transformed to a symmetric self-adjoint (but degenerate) linear equation which is efficiently solved by a diagonally preconditioned conjugate gradient method. For classical fluid flows without collisions, the redistribution step will generate corrections which are of higher order in τ and may be omitted. However, these corrections can become significant in problems with collisions, as demonstrated in [12] for colliding liquid cylinders.

In the liquid region ($\rho = \rho_0$) the additional requirement is implicitly imposed, namely,

$$\frac{\mathrm{d}\rho}{\mathrm{d}t} = \rho_t + \mathbf{u} \cdot \nabla\rho \leq \mathbf{0}. \tag{7}$$

Together with (2), this is equivalent to requiring that

$$\nabla \cdot \mathbf{u} \geq 0 \qquad \text{when} \qquad \rho = \rho_0. \tag{8}$$

This constraint is imposed through the use of the pressure as a Lagrange multiplier. The velocity $\mathbf{u}^{n+1}$ is given by

$$\rho^{n+1}\mathbf{u}^{n+1} = \rho^{n+1}\overline{\mathbf{u}} - \tau\nabla P, \tag{9}$$

where the pressure P solves the variational inequality

$$\tau\nabla\frac{1}{\rho^{n+1}}\nabla P = \begin{cases} \nabla \cdot \overline{\mathbf{u}} & \text{if } P > P_c \\ 0 & \text{if } P = P_c \end{cases}. \tag{10}$$

Note that (10) and (9) imply that $\mathbf{u}^{n+1}$ satisfies (8) when $\rho^{n+1} = \rho_0$. This formulation allows for incipient cavitation regions, where $\rho = \rho_0$, $P = P_c$ and $\nabla \cdot \mathbf{u} > 0$ so that $\rho_t < 0$. In cases where $P > P_c$ so that cavitation is not expected, the inequality in (8) becomes an equality and (9) represents a projection of $\overline{\mathbf{u}}$ onto the space of divergence free velocities. In this case (10) becomes a linear Poisson equation instead of a nonlinear 'obstacle' problem. In either case

the equation is discretized with a finite-element method using either bilinear elements in 2-D or tri-linear elements in 3-D. A structured but generalized grid is used in the 3-D code so the discretization matrix has a simple banded structure. An incomplete Choleski preconditioner is used with the conjugate gradient method to solve the linear system. The same algorithm described above for the density redistribution is used when we impose the pressure constraint for problems where cavitation effects are important.

In the numerical implementation of the generalized hydrodynamic model the new discrete liquid region $\mathbf{D}^{n+1} = \mathbf{D}(t^{n+1})$ is defined to be the collection of grid cells C_l such that

$$\rho_l^{n+1} \geq (1 - \varepsilon_\rho)\rho_0, \tag{11}$$

where $0 < \varepsilon_\rho < 1$. (Note that in our discretization the density and velocity field are defined at the grid cell centers while the pressure is defined at the grid vertex points.) In general, small values of ε_ρ will cause cells with only slightly less density than the liquid to be treated as regions of 'spray' having uniform pressure. Larger values of ε_ρ will cause a larger subset of the region where $0 < \rho < \rho_0$ to be treated as a variable density incompressible region. For all of the computations presented here the value $\varepsilon_\rho = 0{\cdot}1$ was used.

The discrete non-liquid region is divided into evolving disjoint subregions

$$\Omega - \mathbf{D}^{n+1} = \mathbf{A}^{n+1} \cup \mathbf{B}^{n+1} \cup \mathbf{C}^{n+1}, \tag{12}$$

where the 'bubble' domain is further split into connected components

$$\mathbf{B}^{n+1} = \bigcup_{k=1}^{K^{n+1}} B_k^{n+1}. \tag{13}$$

The non-liquid subregions are evolved at each step by checking each cell using (11). For example, consider a cell $C_l \in \mathbf{D}^n$ but $C_l \notin \mathbf{D}^{n+1}$. If C_l is adjacent to one of the non-liquid regions from the previous step, then it is merged with that region. If it is not adjacent to any non-liquid region and $P^n = P_c$ then C_l is included into the cavitation region $C_l \in \mathbf{C}^{n+1}$. Inside the air and cavitation regions, **A** and **C**, the pressure is assumed to be both uniform and constant in time (P_a and P_c, respectively). Since the bubble pressures depend on the volume by an adiabatic law, the individual bubble volumes must be updated at each time step. The volume V_k^{n+1} for bubble B_k^{n+1} is given by

$$V_k^{n+1} = \sum_{C_l \in \overline{B_k^{n+1}}} \left(1 - \frac{\rho^{n+1}}{\rho_0}\right) d_l, \tag{14}$$

where $\overline{B_k^{n+1}}$ is the region B_k^{n+1} together with all cells adjacent to B_k^{n+1}, and d_l is the volume of cell C_l divided by the number of bubbles adjacent to C_l.

At times where the free surface topology is not changing, the bubble pressures are then updated using the adiabatic assumption

$$P_k^{n+1} \left(V_k^{n+1}\right)^\gamma = P_k^n \left(V_k^n\right)^\gamma, \tag{15}$$

The value $\gamma = 1{\cdot}3$ was used for the simulations shown in this paper. This value was selected because it is between typical values given for water vapor $\gamma = 1{\cdot}25$ and air $\gamma = 1{\cdot}4$ and the bubble is assumed to be a mixture of these two gases. The values $\gamma = 1{\cdot}25$ and $\gamma = 1{\cdot}4$ were also tested in simulations but had a relatively small effect on the computed bubble frequencies.

Special algorithms are used in the codes to keep track of bubbles which may merge or split off as well as the treatment of the pressures of merging or splitting bubbles. The details of these treatments have appeared in [22] and [14].

While the computational procedures implemented in the code are second-order accurate in space and time, only first-order accuracy can be expected in determining the locations of the free surfaces since they are captured as discontinuities in density. This first-order rate of convergence has been observed in computations of maximum bubble size, period, and energy losses due to impacts of concentric liquid cylinders in several of the references previously mentioned, *e.g.* [11], [12] or [17].

3. Numerical results

We began our numerical studies approximating the setup shown in Figure 1 as an axially symmetric problem so that the code BUB2D could be used. Three different grid resolutions were used in order to examine grid effects and the numerical accuracy of the simulations. In each case a uniform grid was used in the region $0 \leq r \leq 3R$, $-9R \leq z \leq 0{\cdot}4R$, where $z = 0$ corresponds to the initial air-water surface. Outside of this region the grid is stretched exponentially in the radial direction to $r = R_t = 118{\cdot}48$ cm, down to $z = Z_B = -180$ cm and upward to $z = z_T = 100$ cm, roughly matching the volume and depth of the tank used for the experiments. The cell stretching was performed under the restriction that the ratio of the largest spacing to the smallest was no greater than 20 to 1 in each direction. As mentioned earlier, we will focus on the case where the cylinder has radius, $R = 5{\cdot}4$ cm, and initial height above still water, $H = 15$ cm. In the discussion that follows all distances are measured in units of centimeters (cm) and time is in seconds.

A summary of the grid and simulation parameters for the $L = 45$ case are given in Table 1. The simulations were initialized with the cylinder of water at a height $s_0 = 0{\cdot}108$ cm above the air-water surface, with a velocity specified from its free-fall motion. That is, if the rest configuration shown in Figure 1 corresponds to $t = 0$, we started our computation at time $t_0 = \sqrt{2(H - s_0)/g}$ with the cylinder moving downward with velocity $v_0 = -gt_0$. The simulations were run to time $t = 1{\cdot}5$. These runs were performed on a *Intel Xeon* 1.7 GHz processor using the *Portland Group Fortran* compiler with options (*pgf77 -fast -byteswapio*). In this table, h is the grid size in the region of interest, τ is the time step, and N_r and N_z are the total number of grid cells used in the r and z directions, respectively. For these simulations it can be expected that the execution times would increase by a factor of 16 with each level of refinement. Each refinement level doubles the number of time steps, quadruples the number of cells, and roughly doubles the number of iterations required for the convergence of the solutions to the obstacle problem (5) and pressure equation (10). The execution times listed in Table 1 indeed show an increase by roughly the factor 16 with each refinement.

Figure 2 displays the fine-grid free-surface shapes for the $L = 45$ case at different times in the experiment. At time $t = 0{\cdot}2$ the cylinder has impacted the water surface and a radial plume begins to form around the impact area. This impact phenomenon was studied in detail in [13] where it was shown that just after the impact the liquid velocity behaves asymptotically as $d^{-1/3}$ where d is the distance to the circle on the boundary of the cylinder bottom at the moment of impact with the still water.

Due to the incompressibility assumption and the additional implicit assumption that liquid collisions are inelastic, an energy loss occurs due to the singularity at the moment of impact.

Table 1. Summary of grid parameters and run times for the $L = 45$ case

Grid	h	τ	$N_r \times N_z$	Run Time (hrs:mins:secs)
Coarse	$R/10$	4×10^{-4}	46×144	00:10:54
Medium	$R/20$	2×10^{-4}	92×288	03:20:42
Fine	$R/40$	1×10^{-4}	184×576	48:26:35

If $t_I = \sqrt{2H/g}$ is the time of impact, and $V_I = gt_I$ is the speed of the cylinder an instant before the impact time ($t_I{}^-$), then the energy loss is given by

$$E(t_I{}^-) - E(t_I{}^+) = \pi V_I \int_0^R r I(r, 0) \mathrm{d}r, \tag{16}$$

where $\nabla I(r, z)$ is the pressure impulse imparted to the momentum, and solves the equation

$$\nabla^2 I = -\rho_0 V_I \delta_\Gamma \qquad \text{in} \qquad \mathbf{D}(t_I), \tag{17}$$

$$I = 0 \qquad \text{on} \qquad \partial\mathbf{D}(t_I), \tag{18}$$

with δ_Γ denoting the Dirac 'delta' distribution on $\Gamma = \{(r, z) : z = 0, 0 \leq r \leq R\}$, the disk of intersection of the cylinder with the quiescent surface. The energy loss in this case was computed to be $0{\cdot}01249E(t_I{}^-) = 0{\cdot}001249Mg(H + L/2)$. That is, the energy loss is only approximately 1.25% of the initial potential energy of the water cylinder upon its release. Further discussions on energy losses due to liquid impacts can be found in [23] and the references cited therein. Compressibility effects on fluid impacts, in particular the use of linear acoustics to radiate pressure waves have been studied in [24]. For the case of a triangular wave impact, Cooker [23] used the method of Korobkin [24] to show that the time-averaged compressible velocity field is the same as that predicted by the incompressible pressure impulse theory. This result provides additional justification of the incompressible energy loss described by (16–18) which in turn, is implicitly reproduced by our algorithm.

After the impact, the cylinder opens a cavity as it descends into the water surface at times $t = 0{\cdot}3$ and $t = 0{\cdot}4$. The cavity can be seen collapsing at time $t = 0{\cdot}46$ and at time $t = 0{\cdot}47$ the cavity has closed "pinching off" a bubble. As mentioned in the preceding section, at the moment the bubble is formed, the pressure in the cavity is taken to be the ambient air pressure. Afterwards, the bubble's volume is updated based on the fluid motion and the pressure is determined using the adiabatic assumption (15). At times $t = 0{\cdot}47$ and $t = 0{\cdot}48$ small water jets can be seen moving both upward into the air and downward through the bubble. This phenomenon has been visualized in high-speed photographs of the experiment shown in [3]. The re-entrant jet pierces the bottom of the bubble at $t = 0{\cdot}5$ causing the bubble to change topology to a torus at time $t = 0{\cdot}6$. A second smaller toroidal bubble, formed as the jet travels downward, can also be seen at $t = 0{\cdot}6$. The bubble is rising at $t = 0{\cdot}7$ and vents into the air at $t = 0{\cdot}9$. At time $t = 1{\cdot}37$ several small bubbles remain in the flow field as the upper jet has fallen back down. Note the light-gray regions which can be observed inside the bubble at times $0{\cdot}47 \leq t \leq 0{\cdot}7$. These are regions of simulated spray, which develop near the top of

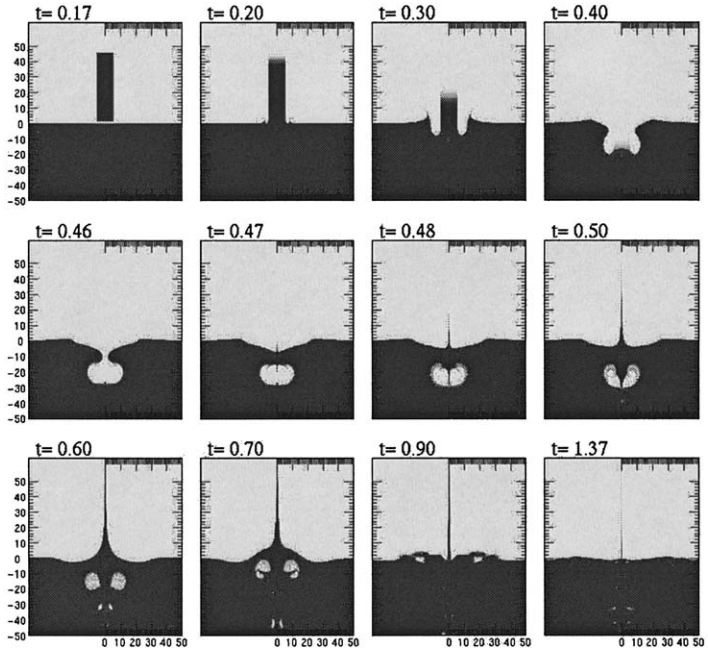

Figure 2. Fine grid BUB2D simulation of the $L = 45$ cylinder impact.

the bubble just before the cavity collapses, and are maintained at each bubble pulsation due to Rayleigh-Taylor instabilities at times when the bubble is near its minimum volume.

Photographs extracted from a video of the $L = 45$ cylinder-impact experiment conducted in an external environment at the Puget Sound [25] are shown in Figure 3 for comparison. The later time images from this video show a significant divergence from axial symmetry due in part to the non-ideal experimental conditions and the unstable nature of the phenomenon, and are not displayed here. The formation of the cavity after the cylinder impacts the air-water surface and the bubble pinch-off are clearly displayed in these photographs. A much more detailed description of this experiment, including images of the cylindrical jet of water above the quiescent surface may be found in [4]. As mentioned previously, high-speed video photographs were presented in [3] showing further details of the bubble formation.

Details of the bubble at a time of 1 ms after the cavity collapses are shown in Figure 4 for each of the 3 grids. The lines delineating the free surface and bubble are density contours with $\rho = \{0{\cdot}1, 0{\cdot}3, 0{\cdot}5, 0{\cdot}7, 0{\cdot}9\}$ (where $\rho_0 = 1$). Velocity vectors are drawn in every fourth cell on the coarse grid (a), every eighth cell on the medium grid (b) and every sixteenth cell on the fine grid (c). On each grid the bubble and air-water surface has approximately the same shape and the velocity vectors are similar. As expected, the contours become sharper as the grid is refined with the exception of the contours on the top (unstable) surface of the bubble which show spreading on each grid. The small 'bump' shown on the bottom of the bubble in the Medium and Fine grid cases were caused by a small bubble entrained during the initial cylinder impact, which rises to the cavity bottom just before it closes. The similarity of these profiles indicate that it is possible to obtain qualitatively realistic simulations using modest computer resources. This will become important in 3-D simulations where the computational requirements are typically 2 to 3 orders of magnitude greater.

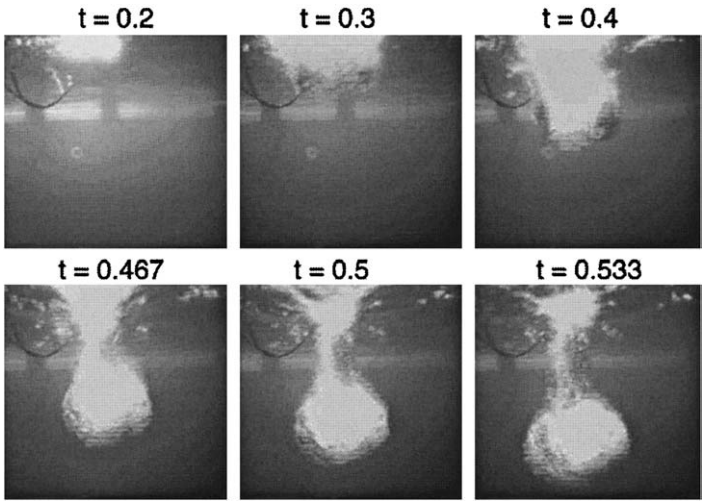

Figure 3. Photographs from video of experiment conducted at Puget Sound for the $L = 45$ case.

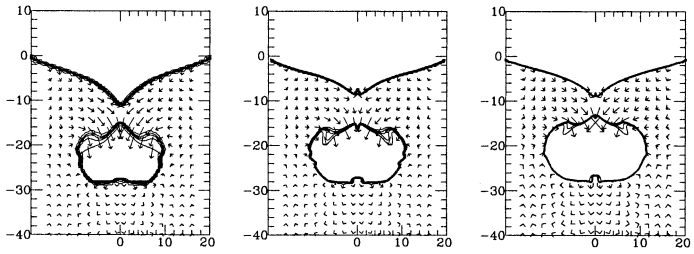

a. Coarse Grid b. Medium Grid c. Fine Grid

Figure 4. Density contours and velocity vectors just after bubble formation.

The quantitative results for the three simulations are shown in Table 2 below. In this table, t_c is the time the cavity collapses, R_b is the equivalent radius of a sphere with the same volume of the bubble at the instant it is created, R_c is the maximum radial extent of the cavity, D is the depth of the cavity at the time of collapse. Also, f_{10} corresponds to the average bubble frequency during its first 10 pulsations, and f corresponds to the frequency of the maximum power spectrum level. The theoretical values listed in Table 2 were computed using [4, Formulae 2,10,14,16 and 25]. (Note, that in [4], time is measured from the time of impact, while we started with the time the cylinder begins to fall). These formulas, together with the determination of the Froude number, F are listed below for convenience.

$$F = \frac{L}{R}\left(1 + 2\frac{H}{L}\right), \qquad t_c = 6F^{-1/6}(R/g)^{1/2}, \tag{19a}$$

$$R_b = 3^{1/3}F^{1/9}, \qquad R_c = \sqrt{3}R, \qquad D = 3RF^{1/3} \tag{19b}$$

The range of values for t_c determined from the experiments were approximated from [4, Figure 11]) for the case when $L/R = 8\frac{1}{3}$. Similarly the range of values for the data for R_b, R_c, and D, were approximated from the data presented in [4, Figures 15, 9, and 12, respectively].

With the exception of the cavity collapse time t_c, where the Coarse and Fine grid values differ by less than 1·3%, the difference in the computed quantities from the Fine and Medium grids were smaller than between the Medium and Coarse grids, indicating the computations

Table 2. Summary of results from simulations with $L = 45$

Grid	t_c	R_b	R_c	D	f_{10}	f
Coarse	0·4697	8·31	10·15	28·88	51·8	51·5
Medium	0·4675	9·33	11·19	28·49	46·3	46·1
Fine	0·4640	9·91	11·63	28·22	44·4	43·8
Theory	0·4621	10·43	9·35	38·94		
Exp. Data Min	0·43	7·3	9·2	27·2	47·6	43
Exp. Data Max	0·50	11·5	11·9	42·8		46

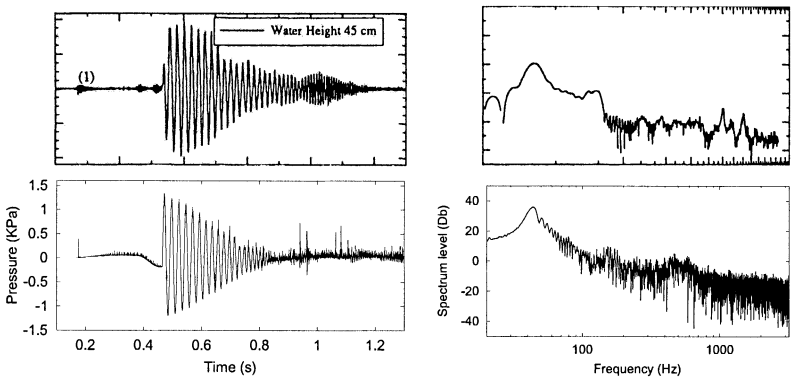

Pressure time series. Power spectral levels.

Figure 5. Computations (bottom) and measurements (top) for the $L = 45$ case.

are converging. All of the computed values are within 2% of the theoretical value for t_c, which itself is close to the average value from the experiments. The computational errors for the value R_b are approximately 5·5%, under the assumption that the values are converging with the same rate that the grid size is decreasing. Extrapolating the Fine grid result would yield an approximation of $R_b = 10{\cdot}49$, which is very close to the theoretical value. While the

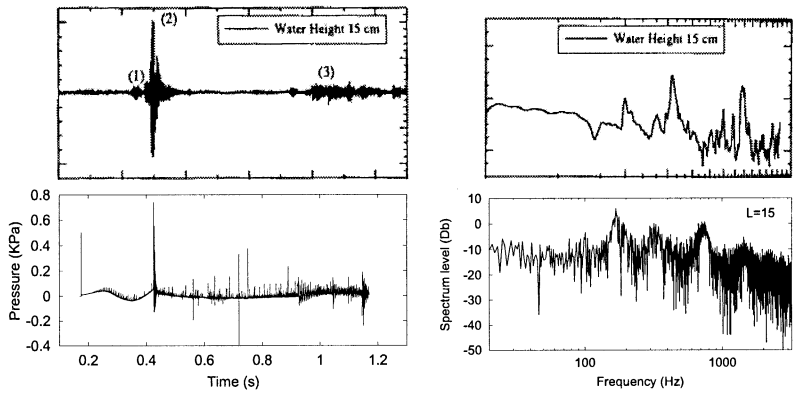

Pressure time series. Power spectral levels.

Figure 6. Computations (bottom) and measurements (top) for the $L = 15$ case.

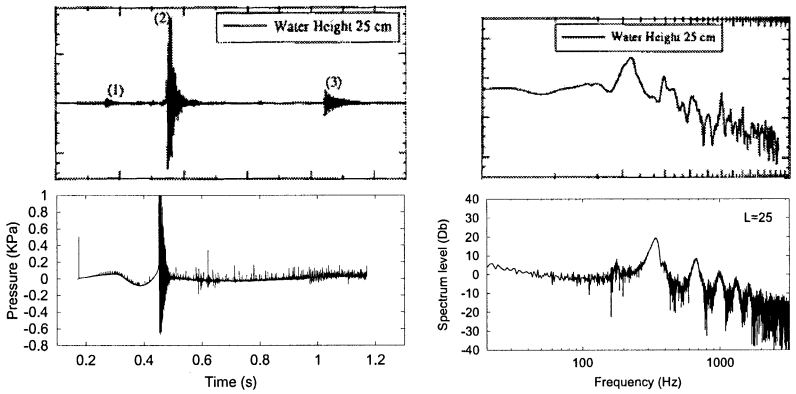

Pressure time series. Power spectral levels.

Figure 7. Computations (bottom) and measurements (top) for the $L = 25$ case.

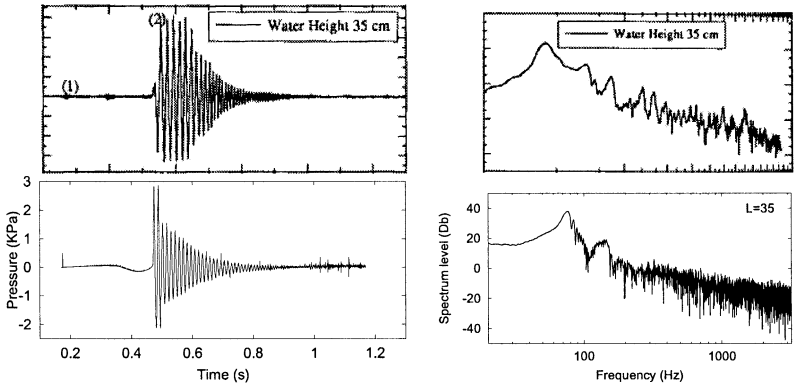

Pressure time series. Power spectral levels.

Figure 8. Computations (bottom) and measurements (top) for the $L = 35$ case.

theoretical value for R_c is within the measured data, it was noted in [4, p. 191] that the estimate $R_c = 2R = 10{\cdot}8$ provided a better match to the data. Here, the computations indicate an extrapolated value of approximately $R_c = 12{\cdot}07$, which is slightly larger than the observations. The cavity depths appear to be on the shallow side of the measured data and well below the theoretical value. The computations using the boundary-integral method in [4] also predicted cavities shallower than those observed. The value, 43 Hz for the fundamental frequency of the pulsating bubble was reported in [3], as well as a bubble radius of $R_b = 11{\cdot}21$ cm. In an earlier note [26] reported the frequency 46 Hz and a bubble radius of 10·2 cm. These two sources were used for the bounds on the fundamental frequency.

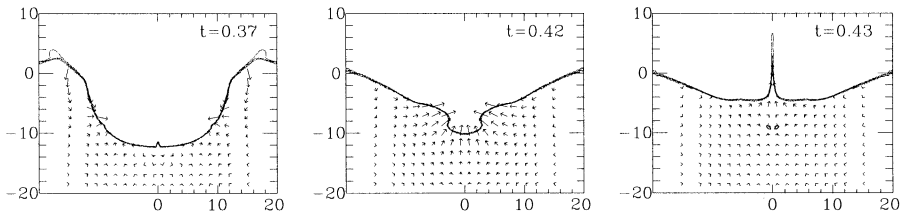

Figure 9. Density contours and velocity vectors for $L = 15$ run.

Table 3. Summary of results from simulations with varying water lengths L

L	t_c	R_b	R_b(data)	f_{10}	f	f(data)
15	0·4250	0·55	1·35	781	171	415
25	0·4510	1·14	4·19	344	348·8	209
35	0·4706	5·50	8·53	75·1	76·9	54

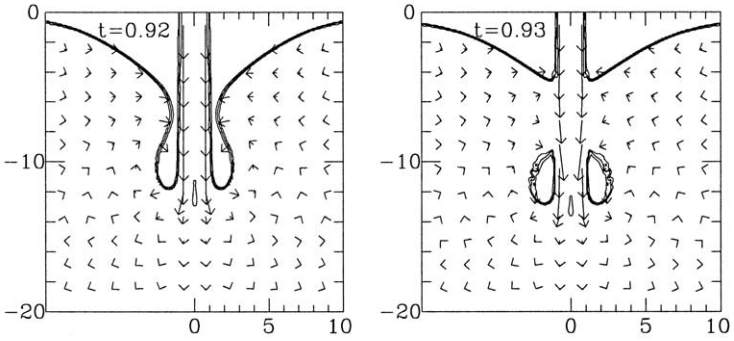

Figure 10. Formation of secondary bubble during jet fall back in $L = 15$ run.

The pressure time history and power spectrum levels are shown in Figure 5 together with the experimental results taken from [3, Figure 4]. The pressure measurements were taken at the location $r = 40$ cm, and $z = -20$ cm. This distance is sufficiently close to the bubble so that the instantaneous propagation of pressure due to the incompressible liquid assumption provides an adequate approximation to the small physical propagation time. In this figure the label '(1)' from the experimental pressure time series corresponds to the time of the initial impact which would correspond to the time $t = \sqrt{\frac{2H}{g}} = 0{\cdot}175$, so that the two plots have approximately the same time scale. The value for f_{10} listed in the 'Exp. Data Min' row of Table 2 was approximated from the experimental results of [3, Figure 4(a)] copied in the upper left graph of Figure 5. The rate of decay of the amplitude of the low-frequency bubble is slightly faster in the computations than in the experiments. This decay occurs in the computations from energy losses due to repeated liquid collisions of water jets forming during the bubble pulsations, as well as numerical dissipation. The spectral level profiles show some similar features, namely, the peak occurring at the fundamental frequency, as well as a lower secondary peak occurring at approximately 180 Hz from the computed data and about 130 Hz in the experimental data, due to the fallback of the plume rising above the air-water surface.

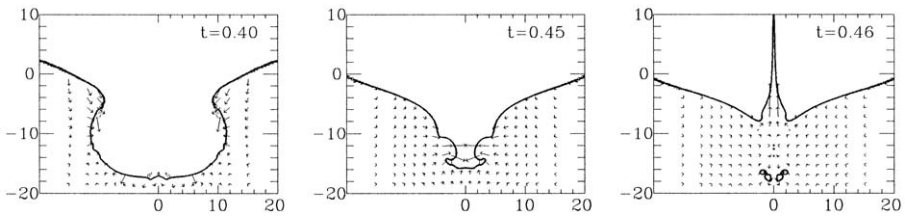

Figure 11. Density contours and velocity vectors for $L = 25$ run.

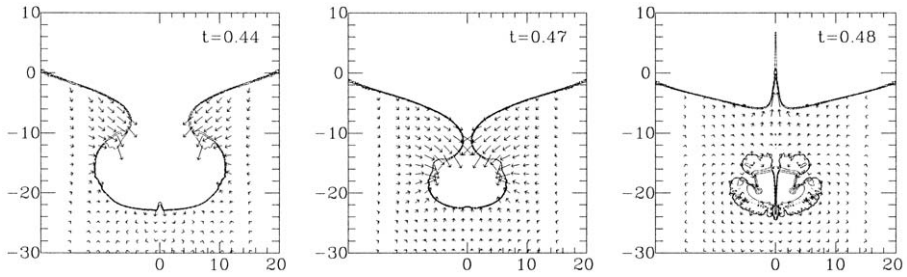

Figure 12. Density contours and velocity vectors for $L = 35$ run.

Next, we turn our attention to cases when the cylinder is shorter, namely $L = 15$, $L = 25$ and $L = 35$. Computations for these three cases used a grid with uniform spacing of size $h = 0{\cdot}1$ cm in the region $0 \leq r \leq 12$ cm, -5 cm $\leq z \leq 4$ cm with grid stretching to the same boundaries as in the $L = 45$ case. The number of cells for this grid was 200×520. Figures 6–8 display the computed pressure time series and power spectrum levels for these cases together with the measurements of [3]. While there are quantitative discrepancies in the frequency predictions, the qualitative agreement of both the time series and power spectral levels in each case is evident. For example, the persistence of the low frequency bubble pulsation in the $L = 35$ case is not retained in the $L = 25$ or $L = 15$ case. The matching of pressure amplitude decay reflects the credibility of the liquid collision energy dissipation mechanisms within our generalized hydrodynamic theory. The similarity in the persistence of the oscillations between the measured and computed time series is remarkable.

Figure 9 shows the contour plots for the $L = 15$ run at various times. The cavity is at its maximum extent at time $t = 0{\cdot}37$. The shape of the cavity just before it collapses occurs at $t = 0{\cdot}42$ and the formation of a small bubble and upward jet just after the collapse are seen at $t = 0{\cdot}43$. Note that the cavity closes in from the bottom and sides at roughly the same speed so that only a very small bubble is formed. The small size of this bubble and the relatively fast closure of the cavity make quantitative predictions of this case difficult. At a later time the fallback of the jet causes another bubble to form as shown in Figure 10 at times $t = 0{\cdot}92$ and $t = 0{\cdot}93$. This bubble is larger, having an initial radius of $2{\cdot}17$ cm and oscillates with a frequency of $f = 171$ Hz, which is the value listed as the fundamental frequency in Table 3. This event was also recorded in the data, and is marked by the label '(3)' in corresponding pressure time series shown in Figure 6.

Contours for the cases $L = 25$ and $L = 35$ are shown below in Figure 11 and Figure 12. As before, these figures show the contours of the cavity near its maximum extent, and just prior and after the cavity collapse. Figure 11 shows that in the $L = 25$ case the cavity closes at a point just above its bottom causing the complex shape seen at $t = 0{\cdot}45$. As in the previous case a small high frequency bubble is formed whose energy is quickly dissipated through subsequent oscillations. The case $L = 35$ is very similar to the case $L = 45$ described above with the exception that the bubble is smaller and pulsates at a higher frequency. Note the unstable nature of the bubble shown at time $t = 0{\cdot}48$ where a water jet is piercing the bubble through the axis, while a second radial jet is penetrating the upper corner. The lack of a sharp outline of the bubble indicates the violent and unstable nature of the bubble pulsations.

A summary of the results is shown in Table 3. In this table the value for R_b is the equivalent radius of the bubble formed at the time of the cavity collapse, where its volume is determined from (14). The measured values for R_b were reported in [3] and correspond to the radii of a

spherical region encapsulating the bubble shape. Void fractions for this region were estimated to range between 32% to 73%, so that the values for R_b(data) in the table should be reduced by factors between 0·68 and 0·9. In these cases the computations predicting frequencies significantly higher than the measurements reported here. However, there was a significant spread in the relation between the measured frequencies and bubble plume radii in the higher frequency regime, (frequencies larger than 100 Hz) so that the $L = 15$ and $L = 25$ data may be particularly difficult to duplicate. However, this does not explain why our errors in frequency in the $L = 35$ case were so much larger than in the similar $L = 45$ case.

4. Conclusions

In this paper we demonstrated that it is possible to predict not only the formation of bubbles formed as the result of liquid impacts, but also the acoustic sources that these bubbles produce as they undergo damped low frequency pulsations. While fairly high resolution (40 cells across the jet diameter) was required to produce frequencies within the range of the experimental data, coarser grids produced results which were qualitatively correct and frequencies within about 15% of the measurements. This is significant because it indicates that 3-D simulations which generally require two or more orders of magnitude more computer resources, are still feasible for simulating realistic jet impact behavior. While our success was not great in predicting frequencies of bubbles when the water jets were shorter, good qualitative agreement between the computed and measured pressure time series was found, in particular, the persistence and decay of the pressure amplitudes. The dominant frequencies were higher in the computations in these cases, but the general structure of the power spectrum level peaks was reproduced.

Acknowledgements

The authors would like to thank Ali Kolaini for introducing us to this interesting and important benchmark problem and for providing the video tape from which the images of Figure 3 were extracted. We also thank the guest editor and reviewers for their helpful comments and suggestions concerning this paper. This work was supported by the Office of Naval Research base funding at the Naval Research laboratory.

References

1. G.B. Deane and M.D. Stokes, Mechanisms in breaking waves. *Nature* 418 (2002) 839–844.
2. M. Loewen, Inside whitecaps. *Nature* 418 (2002) 830.
3. A.R. Kolaini, R.A. Roy, L.A. Crum and Y. Mao, Low-frequency underwater sound generation by impacting transient cylindrical water jets. *J. Acoust. Soc. Am* 94 (1993) 2809–2820.
4. H,N. Oğuz, A. Prosperetti and A.R. Kolaini, Air entrapment by a falling water mass. *J. Fluid Mech.* 294 (1995) 181–207.
5. J.P. Best, The formation of toroidal bubbles upon the collapse of transient cavities. *J. Fluid Mech.* 251 (1993) 79–107.
6. S. Zhang, J.H. Duncan and G.L. Chahine, The final stage of the collapse of a cavitation bubble near a rigid wall. *J. Fluid Mech.* 257 (1993) 147–181.
7. D. Morton, M. Rudman and L. Jong-Leng, An investigation of the flow regimes resulting from splashing drops. *Physics of Fluids* 12 (2000) 747–763.

8. J.C.W. Rogers, Incompressible flows as a system of conservation laws with a constraint. *Seminares IRIA Analyse et Contrôle de Systèmes* (1978) 141–162.
9. J.C.W. Rogers, Energy conservation, and turbulence for water waves. *Seminares IRIA Analyse et Contrôle de Systèmes* (1978) 163–180.
10. J.C.W. Rogers, W.G. Szymczak, A.E. Berger and J.W. Solomon, Numerical solution of hydrodynamic free boundary problems. In: K.-H. Hoffmann and J. Sprekels (eds.), *Free Boundary Problems*. Basel: Birkhäuser Publishing Ltd. (1990) 241–266.
11. W.G. Szymczak, J.C.W. Rogers, J.M. Solomon and A.E. Berger, A numerical algorithm for hydrodynamic free boundary problems. *J. Comp. Phys.* 106 (1993) 319–336.
12. W.G. Szymczak, Energy losses in non-classical free surface flows. In: J. R. Blake, J. M. Boulton-Stone and N. H. Thomas (eds.), *Bubble Dynamics and Interface Phenomena*. Dortrecht: Kluwer Academic Publishers 23 (1994) 413–420.
13. J.C.W. Rogers and W.G. Szymczak, Computations of violent surface motions: comparisons with theory and experiment. *Phil. Trans. R. Soc. London* A355 (1997) 649–663.
14. W.G. Szymczak and J.M. Solomon, Computations and experiments of shallow depth explosion plumes. NSWCDD/TR-94/156, Dahlgren, Virginia: Naval Surface Warfare Center (1996) 76pp.
15. W.G. Szymczak and C.E. Higdon, Model validations and predictions for water barrier defense. NRL/FR/7130–98-9880, Washington, DC: Naval Research Laboratory (1998) 34pp.
16. W.G. Szymczak and J.C.W. Rogers, Generalized hydrodynamics with viscoplasticity for channeling in saturated sand. NRL/FR/7130–00-9946, Washington, DC: Naval Research Laboratory (2000) 27pp.
17. W.G. Szymczak, Simulations of violent free surface dynamics. In: L. K. Leong and T. C. Ann (eds.), *Naval Platform Technology Seminar 2001*. Singapore: Naval Logistics Department, Republic of Singapore Navy (2001) 16-1–16-17.
18. C.W. Hirt and B.D. Nichols, Volume of fluid (VOF) method for the dynamics of free boundaries. *J. Comp. Phys.* 39 (1981) 201–225.
19. D.E. Kothe and R.C Mjolsness, RIPPLE: A new model for incompressible flows with free surfaces. *AIAA J.* 30 (1992) 2694–2700.
20. J.P. Boris, F.F. Grinstein, E.S. Oran and R.J. Kolbe, New insights into large eddy simulation. *Fluid Dyn. Res.* 10 (1992) 199–227.
21. C. Fureby and F.F. Grinstein, Monotonically integrated large eddy simulation of free shear flows. *AIAA J.* 37 (1999) 544–556.
22. W.G. Szymczak, J.M. Solomon, A.E. Berger and J.C.W. Rogers, A numerical method based on a generalized formulation of hydrodynamic free surface problems. In: P. Ruppert and D. Kwak (eds.), *Proceedings of the AIAA 10th Computational Fluid Dynamics Conference*. AIAA-91-1541-CP, Honolulu, Hawaii: American Institute of Aeronutics and Astronautics (1991) 155–165.
23. M.J. Cooker, Liquid impact, kinetic energy loss and compressibility: Lagrangian and Eulerian and acoustic viewpoints. *J. Engng. Math.* 44 (2002) 259–276.
24. A.A. Korobkin, Global characteristics of jet impact. *J. Fluid Mech.* 307 (1996) 63–84.
25. A.R. Kolaini, R.A. Roy and D.L. Gardner, Low-frequency acoustic emmisions in fresh and salt water. *J. Acoust. Soc. Am.* 96 (1994) 1766–1772.
26. A.R. Kolaini, R.A. Roy and L.A. Crum, An investigation of the acoustic emissions from a bubble plume. *J. Acoust. Soc. Am.* 89 (1991) 2452–2455.